

# MFIT : Multi-Fidelity Thermal Modeling for 2.5D and 3D Multi-Chiplet Architectures

LUKAS PFROMM\* and ALISH KANANI\*, University of Wisconsin–Madison, USA

HARSH SHARMA, Washington State University, USA

PARTH SOLANKI and ERIC TERVO, University of Wisconsin-Madison, USA

JAEHYUN PARK, University of Ulsan, Republic of Korea

JANARDHAN RAO DOPPA and PARTHA PRATIM PANDE, Washington State University, USA

UMIT Y. OGRAS, University of Wisconsin–Madison, USA

Rapidly evolving artificial intelligence and machine learning applications require ever-increasing computational capabilities, while monolithic 2D design technologies approach their limits. 2.5D/3D heterogeneous integration of smaller chiplets using advanced packaging has emerged as a promising paradigm for addressing this limit and meeting performance demands. These approaches offer a significant cost reduction and higher manufacturing yield than monolithic 2D integrated circuits. However, the compact arrangement and high compute density of these systems exacerbate thermal management challenges, potentially compromising performance. Addressing these thermal modeling challenges is critical, especially as system sizes grow and different design stages require varying levels of accuracy and speed. Since no single thermal modeling technique meets all these needs, this paper introduces MFIT, a range of *multi-fidelity thermal models* that effectively balance accuracy and speed. These multi-fidelity models can enable efficient design space exploration and runtime thermal management. Our extensive testing on systems with 16, 36, and 64 2.5D integrated chiplets and 16×3 3D integrated chiplets demonstrates that these models can reduce execution times from days to mere seconds and milliseconds with negligible loss in accuracy.

## ACM Reference Format:

Lukas Pfromm, Alish Kanani, Harsh Sharma, Parth Solanki, Eric Tervo, Jaehyun Park, Janardhan Rao Doppa, Partha Pratim Pande, and Umit Y. Ogras. 2025. MFIT : Multi-Fidelity Thermal Modeling for 2.5D and 3D Multi-Chiplet Architectures. 1, 1 (February 2025), 24 pages. <https://doi.org/XXXXXXX.XXXXXXX>

## 1 INTRODUCTION

Massive data from different modalities, including text, images, video, and speech, are continuously produced by various sensors. At the same time, increasingly complex artificial intelligence (AI) and machine learning (ML) algorithms process this data to enable new applications that were previously impractical. This trend dictates the design of large-scale chips with high memory and compute capabilities, offering a high degree of parallelism [3, 6]. Traditional 2D chip design and packaging technologies cannot sustain this need due to the low yield of large

\*Both authors contributed equally to this research.

Authors' addresses: Lukas Pfromm, [pfromm@wisc.edu](mailto:pfromm@wisc.edu); Alish Kanani, [ahkanani@wisc.edu](mailto:ahkanani@wisc.edu), University of Wisconsin–Madison, Madison, Wisconsin, USA; Harsh Sharma, Washington State University, Pullman, Washington, USA; Parth Solanki; Eric Tervo, University of Wisconsin-Madison, Madison, Wisconsin, USA; Jaehyun Park, University of Ulsan, Ulsan, Republic of Korea; Janardhan Rao Doppa; Partha Pratim Pande, Washington State University, Pullman, Washington, USA; Umit Y. Ogras, University of Wisconsin–Madison, Madison, Wisconsin, USA.

Permission to make digital or hard copies of all or part of this work for personal or classroom use is granted without fee provided that copies are not made or distributed for profit or commercial advantage and that copies bear this notice and the full citation on the first page. Copyrights for components of this work owned by others than the author(s) must be honored. Abstracting with credit is permitted. To copy otherwise, or republish, to post on servers or to redistribute to lists, requires prior specific permission and/or a fee. Request permissions from [permissions@acm.org](mailto:permissions@acm.org).

© 2025 Copyright held by the owner/author(s). Publication rights licensed to ACM.

XXXX-XXXX/2025/2-ART \$15.00

<https://doi.org/XXXXXXX.XXXXXXX>

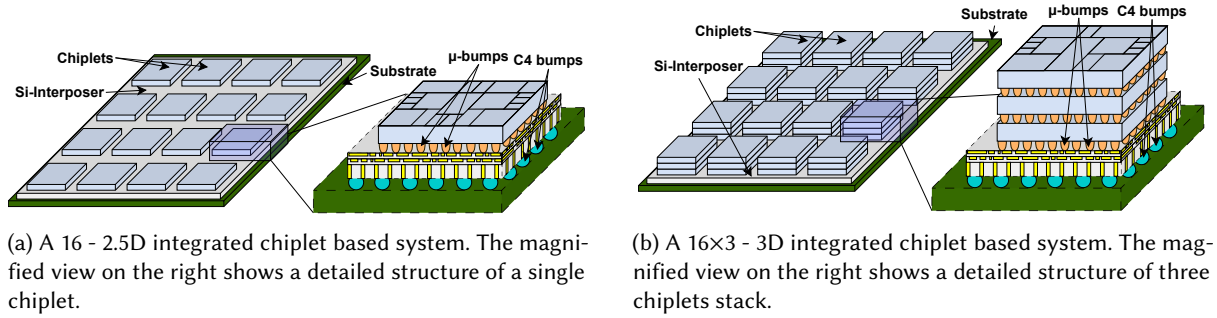


Fig. 1. 2.5D and 3D integrated chiplet systems considered in this work, showing the chiplets, interposer, and a portion of the substrate.

monolithic planar chips and the corresponding increase in fabrication cost [14]. Therefore, new design approaches are required to meet the increasing demand for computing power and memory capacity [3].

2.5D and 3D chiplet-based architectures have emerged as promising alternatives to traditional monolithic 2D chips due to their lower fabrication costs [28, 44, 48]. Compared to conventional monolithic systems, chiplet-based systems integrate multiple small pre-fabricated chips (chiplets) on a silicon interposer, which facilitates data exchange, as illustrated in Figure 1a. 3D packaged systems expand on this approach by stacking multiple chiplets vertically and connecting them with vertical vias, creating a more compact system as illustrated in Figure 1b. The smaller size of these chiplets enables a higher yield and lower overall manufacturing cost than traditional monolithic dies [53]. Additionally, this modular approach facilitates scaling the system sizes and enables heterogeneous integration of different chiplet types, e.g., memory, processing, and processing-in-memory chiplets. Hence, emerging 2.5D and 3D architectures enable a new cost-effective avenue for compact scale-out implementations of various emerging compute- and data-intensive applications, including AI/ML. Indeed, these advantages have led to industrial adoption by companies including Intel [10, 56], AMD [4, 8, 39], and NVIDIA [44].

Thermal bottlenecks have long been a significant barrier to increasing the performance of computing systems. 2.5D and 3D integrated systems exacerbate this barrier due to their dense integration and unique physical structure [42]. In contrast to a monolithic chip, where heat is spread directly across the die, a 2.5D chiplet-based system conducts heat between different chiplets through the interposer and heat spreader. Likewise, heat also flows vertically between adjacent stacked chiplets in a 3D chiplet-based system.

These factors introduce unique challenges for effective thermal management in these systems. Traditional design flows and physical floorplanning focus on reducing wire lengths to meet timing constraints and minimizing area to reduce fabrication costs. However, these objectives could also lead to thermal crosstalk, thermal hotspots, and compromise performance. Chiplet-based systems introduce additional design parameters such as inter-chiplet link length, spacing, chiplet placement, sizing, inter-layer communication, and design partitioning. Tuning traditional and chiplet-based design parameters while maintaining thermal stability is critical to ensure a thermally-efficient design.

The semiconductor chip design cycle spans multiple phases: system specification, architecture exploration, logic design, physical design and validation, fabrication, and post-silicon optimization/validation. Each phase has a unique set of design constraints and requirements. For example, the lack of a test chip during the pre-silicon phases requires simulation and analytical models. Finite Element Method (FEM) simulations offer the most accurate approach for pre-silicon thermal analysis [54]. They can serve as a reference and enable heat flow studies to guide the design process. However, they are too slow for practical architecture and design space exploration (DSE), as illustrated in Figure 2. Modeling the package as a thermal RC (resistive-capacitive) network

	FEM Models		Analytical Models	
	1. Fine-grained	2. Abstracted	3. Thermal RC Model	4. Discrete State-Space (DSS)
<b>Features</b>	Most accurate (e.g., real μbumps, links geometries)	Replaced micro-structures with equivalent material blocks	Independent of specific geometry, continuous time	Tuned for a specific architecture, discrete time
<b>Error</b>	Golden reference	< 0.5 °C	< 1.7 °C	Same as thermal RC
<b>Exe. time</b>	Not possible to model entire package	Days	Seconds	Milliseconds
<b>Use case</b>	Validate the abstracted FEM models	Ground truth to tune C values in Thermal RC model	Thermal-aware DSE, reference for DSS model	Large-scale optimization, thermal management
<b>Described in</b>	Section 3	Section 4.2	Section 4.3	Section 4.4

Fig. 2. Summary of the multi-fidelity thermal models. (1) Fine-grained FEM models capture precise geometry but are too complex to simulate the entire chiplet-based system. (2) Abstracted FEM models are derived from the fine-grained model to simulate large-scale systems with negligible impact on accuracy ( $< 0.5^{\circ}\text{C}$ , which is 0.5–1% around the temperatures of interest). (3) Since abstract FEM models are still too slow for DSE, they are used to tune thermal RC circuit models, which introduce less than  $1.7^{\circ}\text{C}$  (1–3.5% around the temperatures of interest) error). (4) Further abstraction reduces the execution time to milliseconds using DSS models developed for specific system configurations, enabling runtime thermal management.

can significantly accelerate simulations with acceptable accuracy loss [49, 52]. Since each node in the thermal circuit corresponds to a specific location in the package, thermal RC models solve discretized versions of the FEM models *in space*. Hence, they enable thermally-aware DSE and optimization with a finite number of discrete hotspot nodes. However, the thermal resistance/capacitance values and the circuit topology must accurately reflect the chip geometry and material properties for reliable results. Since the thermal RC models solve continuous-time ordinary differential equations (ODEs), they have execution times in the order of seconds to minutes. Therefore, they cannot be used for runtime optimization tasks such as dynamic thermal and power management (DTPM). With a given sampling period, one can discretize them *in the time domain*. The resulting discrete state-space (DSS) models significantly reduce runtime *at the cost of further abstracting the model from the physical package*. Consequently, they apply only to the specific configurations for which they are developed.

There is a strong need for tools to accurately analyze the thermal behavior of 2.5D and 3D integrated systems and guide their design process. However, no single modeling technique can alone address the needs of all design phases. To address this critical gap, this paper proposes MFIT, a *multi-fidelity thermal modeling framework* that synergistically exploits the strengths of each class of models (FEM, thermal RC, and DSS). We use this framework to produce a set of thermal models that can guide the entire design cycle, unlike a point solution that can serve a specific portion of the design process. *The elements of this set not only cover complementary parts of the design cycle but support each other and produce consistent results.* We first develop a fine-grained FEM model of the target package as a reference. Since it is slow and computationally expensive, we next judiciously design an abstracted version of this fine-grained FEM model to simulate an entire package in days while maintaining accuracy. To enable fast DSE, MFIT also incorporates thermal RC circuit models verified against the reference FEM models. Our thermal RC models run in the order of seconds while leading to less than  $1.7^{\circ}\text{C}$  error when the package temperature is around  $100^{\circ}\text{C}$ , as summarized in Figure 2. Hence, they can be used for pre-silicon architectural optimization, such as mapping the workloads to chiplets, network-on-interposer design, and chiplet placement for 2.5D and 3D stacked systems. Finally, MFIT derives a final class of models by discretizing the thermal RC models, enabling runtime thermal management and large-scale DSE in the order of milliseconds. Since these discrete models are generated for a specific sampling period and configuration, they are regenerated from the RC model if the target configuration changes *automatically in a few milliseconds*. In summary, we obtain a set of multi-fidelity thermal models that guide and complement each other to cover all design phases.

The key contributions of this work are as follows:

- A novel thermal modeling approach that systematically abstracts fine-grained FEM models to produce abstract FEM, thermal RC, and DSS models to achieve varying speed and accuracy trade-offs,
- A family of *open-source multi-fidelity thermal models* that span a broad accuracy (reference to 1.7°C) and speed (days to milliseconds) range,
- Extensive evaluations with 16, 36, and 64 - 2.5D and 16×3 - 3D integrated chiplets systems running AI/ML workloads to demonstrate the accuracy and speed-up benefits of our multi-fidelity thermal models,
- Open-sourced code for thermal RC and DSS models at [github.com/AlishKanani/MFIT](https://github.com/AlishKanani/MFIT). The FEM models created for this work are included as well.

The remainder of the paper is organized as follows. Section 2 and Section 3 discuss related work and background on FEM. Section 4 presents the proposed multi-fidelity thermal modeling framework. Finally, Section 5 presents the experimental evaluation, and Section 6 concludes the paper.

## 2 RELATED WORK

2.5D and 3D integration-based systems are becoming mainstream due to higher performance and lower manufacturing costs than monolithic chips. Both domain-specific and general-purpose 2.5D and 3D architectures have been explored to date [4, 8, 18, 27, 44, 47, 48]. SIMBA is one of the first prototype multi-chip modules with 36 chiplets designed for inference with deep models [44]. Similarly, Floret is a data center-scale architecture for accelerating convolutional neural network (CNN) inference tasks by exploiting dataflow patterns [48]. Loi et al. [35] analyze the performance benefits of vertically integrated (3D) processor-memory hierarchy under thermal constraints. Similarly, Eckert et al. [18] consider processing-in-memory (PIM) architectures implemented using 3D die stacking. They study the thermal constraints across different processor organizations and cooling solutions to identify viable solutions. Our proposed open-source thermal models catalyze similar thermal analysis and optimization studies for 2.5D and 3D integrated systems.

The most accurate and direct thermal evaluation approach is temperature measurements on a hardware system. It can be performed using thermal imaging [5, 43] or temperature sensors [60, 61]. However, the availability of the target hardware is a significant limitation. For example, large-scale 2.5D and 3D chiplet systems with tens of chiplets do not exist yet, while smaller prototypes and commercial systems provide limited insights applicable for larger systems [39, 59]. This limitation motivated FEM-based modeling as the most accurate way to analyze the heat flow and temperature [54]. Proprietary software, such as ANSYS Fluent [37] and COMSOL [16], are commonly used for FEM simulations. Since FEM suffers from computational cost, detailed FEM solutions are suitable only for small designs and validating analytical models [37]. For example, the authors of [63] employ FEM to simulate a two-chiplet system on an interposer. They employ abstracted FEM models for both  $\mu$ -bumps and C4 bumps to speed up the process, effectively reducing computational complexity before tackling the entire system.

The computational overhead and impractically high execution time of FEM solvers motivate analytical models that enable rapid thermal evaluation in early design phases. The most common method involves constructing thermal RC networks and solving the corresponding system of ODEs. Popular thermal simulators such as HotSpot [49] leverage this method, focusing on the microarchitectural layout blocks to facilitate design space exploration and early-stage thermal-aware layout and placement. Similarly, 3D-ICE [52] models liquid cooling with microchannels embedded between silicon layers. PACT [57] also employs a similar methodology by utilizing SPICE tools as solvers, focusing on standard-cell-level thermal analysis for 2.5D systems. However, these tools lack essential features required for accurately modeling chiplet-based heterogeneous systems and are not fast enough for large-scale, thermally-aware design space exploration (DSE) of multi-chiplet 2.5D and 3D integrated systems, as summarized in Table 1 and detailed next.

Table 1. Qualitative analysis of existing analytical thermal models and our proposed thermal RC and DSS models. Quantitative runtime comparison is completed in Section 5

	Non-uniform grid	Anisotropic materials	Non-homogeneous layers	Heat dissipation from both boundaries of the package	Flexible with Architecture changes
Hotspot [50]	×	×	✓	✓	✓
PACT [57]	×	×	✓	×	✓
3D-ICE [52]	✓	×	×	× <sup>1</sup>	✓
Thermal RC	✓	✓	✓	✓	✓
DSS	✓	✓	✓	✓	×

2.5D and 3D packages often involve materials with varying thermal conductivity across different directions. For example, the thermal conductivity of the C4 layer is higher in the vertical direction than in the lateral direction. The existing thermal models [49, 52, 57] do not account for these anisotropic properties. Moreover, [49, 57] assume a uniform grid size for all material layers (e.g., interposer, C4 bumps, chiplets). Non-uniform grids are useful for simulating regions with substantial spatial variation in temperature without unnecessarily increasing computational costs for simulating regions of moderate temperature variation. While 3D-ICE supports non-uniform grids for 3D architectures, it does not allow non-homogeneous layers, where different regions within the same layer can have distinct material properties. This limitation is particularly significant for emerging technologies, such as active interposer-based systems where chiplets are embedded [55]. *In contrast, our multi-fidelity models address these limitations by enabling variable thermal conductivity across different directions and allowing flexible grid sizes for each layer and block.* Additionally, our models support heat dissipation from both package boundaries, a crucial aspect overlooked by some existing approaches. This capability is essential for accurately modeling advanced cooling techniques, such as immersion cooling systems and flip-chip packages, which rely on efficient heat dissipation through both package boundaries to maintain optimal performance and reliability [22, 34]. Table 1 provides a detailed qualitative comparison of existing thermal modeling tools. *Detailed quantitative runtime comparisons between MFIT and state-of-the-art approaches are presented in Section 5.*

Architecture-level thermal RC models are commonly used for offline studies. For example, temperature sensor placement requires using a thermal model [15, 58]. Similarly, thermally-aware chiplet placement techniques in [19, 32, 36] rely on the use of architectural thermal simulators to optimize the placement of chiplets and identify possible hotspots. While existing simulators can provide the functionality required for these studies, their prohibitive runtime prevents more extensive evaluations from being performed. Faster thermal simulation tools that do not sacrifice accuracy are required to enable more comprehensive work.

However, existing architectural simulators are inadequate for dynamic thermal and power management (DTPM). DTPM requires a much faster temperature estimation time, on the order of milliseconds, for real-time temperature management [9, 45]. DSS models address this need by deriving a discrete-time linear time-invariant system that models the thermal dynamics at fixed locations as a function of the power consumption. For instance, TILTS [20] discretizes the power inputs to the chip over fixed time intervals to accelerate thermal simulations. Hence, it needs to be reproduced when the timing requirements or the underlying hardware configuration change. The speedup gain offsets the loss of the explicit connection to the hardware parameters (e.g., thermal conductance and capacitance) and generality.

The results of FEM, thermal RC, or other thermal simulations can also be used to train physics-informed machine learning techniques to model heat transfer in integrated circuits to reduce the thermal modeling effort [12]. For example, a recent technique collects data from numeric simulations and trains a random forest

<sup>1</sup>With Non-uniform grid, 3D-ICE does not support secondary heat flow path.

model to predict the convection heat transfer coefficients for a nonlinear heat transfer problem [29]. Similarly, Hwang et al., [24] present closed-form models derived from numerical simulations for tapered micro-channels to analyze the heat transfer performance as a function of the channel geometry. In contrast to individual classes of thermal models, this work proposes a framework to produce *a family of multi-fidelity thermal models for 2.5D and 3D chiplet-based systems*. The specific set of models designed with this framework covers a wide range of accuracy and execution time trade-offs, making them suitable for different design phases. Additionally, they can be augmented by additional models, such as physics-informed ML models, with complementary accuracy and execution time trade-offs.

### 3 FINITE ELEMENT METHOD FOR THERMAL ANALYSIS

FEM analysis begins by dividing the problem domain into small finite elements, converting the continuous governing partial differential equations (PDEs) into algebraic equations. Next, the system's geometry is broken down into a lattice of small discrete cells called a “mesh” which approximates a larger, continuous block [37]. After applying the PDEs and boundary conditions to each element, the equations are assembled into a global algebraic system, maintaining continuity between adjacent elements. This global system, representing the discretized PDEs over the whole domain, is solved numerically for the field variables at each mesh node. In this work, only the equation governing solid conduction is solved [54]:

$$\nabla \cdot [k \nabla T] + \dot{q} = \rho C_v \frac{\partial T}{\partial t} \quad (1)$$

where  $k$  is the thermal conductivity,  $T$  is the temperature,  $\dot{q}$  is the heat generation rate,  $\rho$  is the density, and  $C_v$  is the volumetric specific heat.

#### 3.1 Stages of the FEM Simulation Pipeline

Performing FEM simulations involves several key processing steps visualized in Figure 3. First, the geometry, a 3D representation of the 2.5D or 3D integrated package, is created using computer-aided design tools. While increasing the detail in the geometry allows for more accuracy in modeling the system, it also increases the simulation time. This geometry should be as detailed as possible while allowing the setup and simulation to be completed within the given time constraints. Next, a volumetric mesh is generated by transforming the 3D model into one consisting of many individual cells on which the FEM software operates. A mesh sensitivity study is performed to determine if the mesh quality is sufficient. In this process, simulations are run with a progressively finer mesh while output parameters (such as temperature) are monitored. The mesh quality is considered to be sufficient when increasing the mesh granularity no longer impacts the temperature output.

Once an acceptable mesh has been created, it is imported into the solver. The simulation is then set up, including boundary conditions, material parameters, power source terms, and other general model parameters. Our specific system setup is expanded upon in Section 5. Finally, the FEM software simulates the model by solving the governing equations.

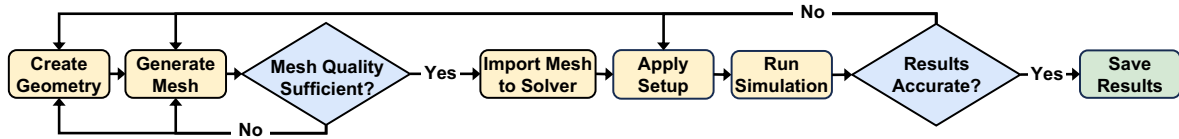


Fig. 3. An illustration of the FEM pipeline.

### 3.2 Impracticality of FEM Simulations

While FEM simulations offer high accuracy, they are impractical for DSE or runtime thermal management due to their time-consuming setup and operation. The process of geometry creation, meshing, solver setup, and execution is intricate and often exceeds the simulation runtime itself. Because the simulation process requires multiple iterations for reliable results, this time overhead quickly becomes prohibitive. The setup of 2.5D or 3D integrated systems is especially complex due to the large number of discrete power sources. These systems also involve numerous small and large bodies, dramatically increasing the computational complexity and the solver runtime [37]. Simulation times range from hours to days, directly impacted by geometric detail, complexity, size, and setup parameters such as the time step. Consequently, analyzing 2.5D or 3D integrated systems with intricate geometries and operating conditions using FEM simulations becomes prohibitively time-consuming, highlighting the need for alternative approaches.

## 4 MULTI-FIDELITY THERMAL MODELING

### 4.1 Overview of the Proposed Approach

Our multi-fidelity thermal model set involves four individual models, visualized in Figure 4. The process of creating these models is identical for any packaging technology. In this work, we consider 2.5D chiplet on silicon interposers and 3D systems integrated with  $\mu$ -bumps [4, 31]. MFIT supports other integration methods and packaging technologies as well, as described below.

We start by creating fine-grained FEM models of specific components within the package. For example, we model individual links within the interposer and  $\mu$ -bumps which are used to connect chiplets to the interposer and between 3D stacked chiplets. The cost of this level of detail is the model complexity and execution time that limits the simulation scope. Therefore, these fine-grained models are used as a reference to design abstracted FEM models, as explained in the following subsection. This abstraction enables system-level FEM simulations of systems with significantly higher chiplet counts than would otherwise be possible, with negligible accuracy loss. All FEM simulations are performed using ANSYS Fluent [37]. The third class of model in the MFIT framework is the thermal RC model. Since these models are constructed using the geometry and material parameters of the

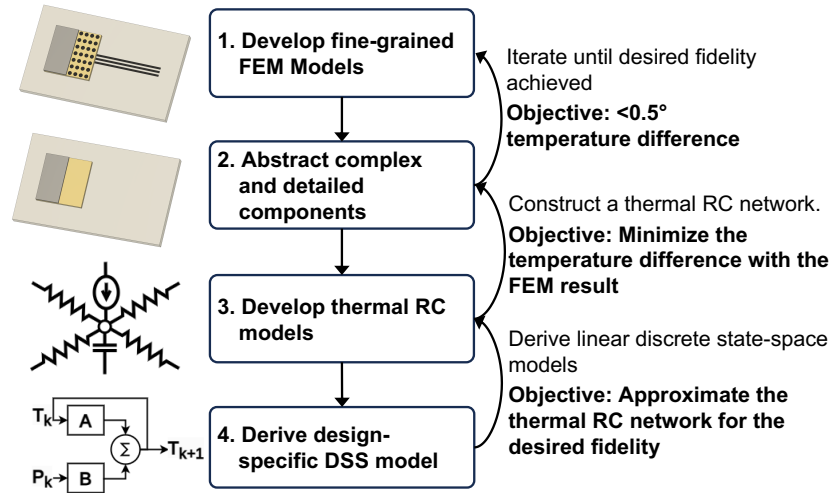


Fig. 4. Flow diagram of MFIT, the proposed multi-fidelity thermal modeling framework.



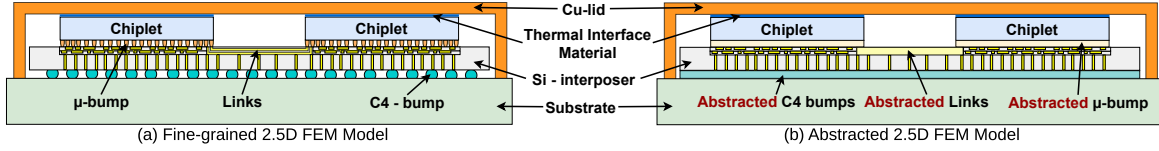


Fig. 5. Cross section of a 2.5D integrated system on Si-interposer showing abstracted blocks for the  $\mu$ -bumps, C4 bumps, and link structures.

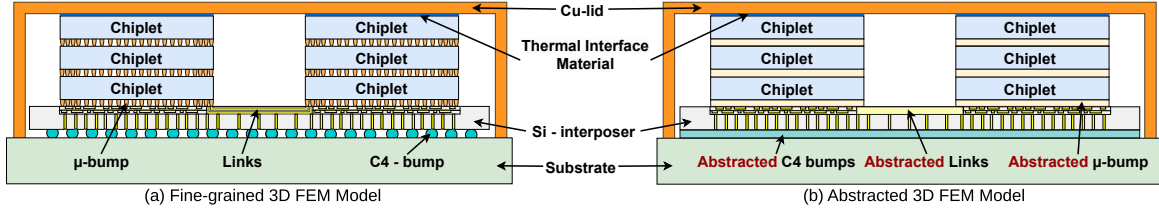


Fig. 6. Cross section of a 3D integrated system showing abstracted blocks for the  $\mu$ -bumps, C4 bumps and link structures.

system, a new RC model of a different system configuration can be created without re-running FEM simulations, allowing for rapid DSE. Finally, the continuous-time state-space equations that govern the thermal RC models are discretized with a given sampling period to create DSS models as detailed in Section 4.4.

## 4.2 Fine-Grained to Abstracted FEM Modeling

First, fine-grained models of key system components are constructed with as much detail as possible. Fine-grained modeling of the entire system at the highest level of detail is infeasible due to the memory, CPU, and execution time requirements. The second step is systematically designing abstracted models by replacing detailed structures with homogeneous blocks. During this process, we find the material parameters for these blocks such that their thermal behavior matches the original structure.

MFIT focuses on two structures within a chiplet-based package for this work: the  $\mu$ -bumps connecting each chiplet to the interposer and 3D stacked chiplets to each other and the links that enable communication between chiplets. The rationale behind selecting these components is elaborated on in the following subsections. These two structures are present in both 2.5D and 3D chiplet-based packages, as shown in Figures 5 and 6, and the results of the abstraction experiments are applied to both the 2.5D and 3D full-system abstracted models.

While we apply our abstract modeling approach to only two structures in this work, the same approach applies to other structures in the package, such as the substrate or C4 bumps. In addition to these abstractions, MFIT also models the heatsink as a heat transfer coefficient (HTC) instead of a physical model. This choice removes the need to model fluids in our simulations, as fluid flow in our simulations is used only for convective heat transfer in the heatsink.

**4.2.1  $\mu$ -bump Abstracted Model.** The  $\mu$ -bumps are particularly important for thermal behavior due to their placement in the 2.5D and 3D integrated systems. In the 2.5D system, the  $\mu$ -bumps are one of two paths to dissipate heat from a chiplet, as illustrated in Figure 5. Similarly, in the 3D system, all heat flow for the lower two chiplets in each stack must travel through one of two  $\mu$ -bump layers, as shown in Figure 6. Due to the density and the total number of  $\mu$ -bumps present, which number in the thousands, it is impractical to simulate an entire package with individually modeled  $\mu$ -bumps in FEM. Therefore, a small block of the  $\mu$ -bump layer, along with the



associated upper and lower layer, is simulated in isolation to determine thermal properties that can be applied to the final abstracted models as illustrated in Figure 7.

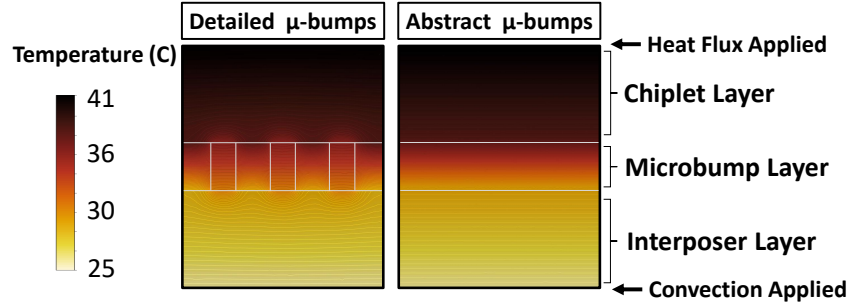


Fig. 7. Temperature contour of a  $\mu$ -bump layer subsection.

First, the detailed block containing  $\mu$ -bumps and underfill material is simulated with static heat flux and convection boundaries, which are applied to create a measurable thermal gradient across the  $\mu$ -bump layer. Then, the thermal conductivity  $k$  is calculated as:

$$k = \frac{\dot{q} \cdot l}{A \cdot \Delta T} \quad (2)$$

where  $\dot{q}$  is the heat flow rate,  $l$  is the thickness of the material,  $A$  is the cross-sectional area, and  $\Delta T$  is the temperature difference across the material [41]. Thermal capacitance and specific heat are calculated via weighted body average [30]. These parameters are applied to a model containing a homogeneous block in place of the previously modeled  $\mu$ -bumps and underfill material. Finally, the same boundary conditions are used, as shown in Figure 7.

We observe identical temperature drop across the  $\mu$ -bump layer of the abstracted model and less than a tenth of a degree difference in interface temperatures in this sub-block, as presented in Table 2, while achieving approximately 1.5x speedup.

Table 2. Temperature results of the  $\mu$ -bump block abstraction experiments. Only a single result is shown for brevity.

Model	Upper surface Temp. (°C)	Lower surface Temp. (°C)	Temp. Drop (°C)
Detailed $\mu$ -bumps	39.13	31.05	8.08
Abstracted $\mu$ -bumps	39.26	31.18	8.08

**4.2.2 Link Abstracted Model.** A link is a group of wires embedded in the interposer to interconnect chiplets. Depending on the thermal crosstalk over the links, the NoI architecture can significantly affect a system's thermal behavior. To determine how links are modeled in the complete system simulations, we tested three different configurations of a two-chiplet package. These configurations model the link (1) in full detail, (2) as an abstracted block, and (3) not included at all. We use two different power configurations: (a) the power dissipation is static over time, and (b) it varies dynamically over time. These power consumption profiles are applied to one chiplet while the temperature of the other chiplet is calculated through FEM simulation. The mean absolute error (MAE) of the receiving chiplet temperature compared to the detailed model case is recorded in Table 3. Only a minimal accuracy loss is observed for both cases, while execution time savings are significant, as shown in Table 4. Therefore, we choose not to model links in our full-system simulations.

Table 3. Error comparison between abstracting and removing the links compared to detailed link modeling while operating between 60 to 100 °C.

Power	Steady MAE (°C)	Transient MAE (°C)
<b>Abstracted links</b>	0.05	0.02
<b>No links</b>	0.34	0.13

Table 4. Execution time for Detailed, Abstract, and No Links experiments with steady and transient power inputs.

Power	Steady Exe. time (min)	Transient Exe. time (min)
<b>Detailed links</b>	489.23	503.86
<b>Abstract links</b>	164.29	172.64
<b>No links</b>	123.80	132.13

**4.2.3 Heatsink Abstracted Model.** FEM simulations that involve a heatsink must model the convective heat transfer from the system to the atmosphere using fluid models [63]. However, modeling the fluid dynamics dramatically increases the setup and runtime of FEM simulations. Additionally, the geometry must be modified for every different heatsink configuration, further increasing the time needed for design iteration. Due to their complexity, high-performance cooling methods, such as liquid cooling, are also difficult to model in FEM-based simulations.

In MFIT, we remove the need to model the heatsink by abstracting the cooling solution to a single HTC. This coefficient is applied to the top of the lid where a heatsink is typically attached. Modeling a heatsink as a HTC is a common practice for many different cooling solutions [26, 40]. This approach allows for a great deal of flexibility in FEM modeling. Instead of completing the time-consuming pipeline in Figure 3, the HTC can be easily modified to test the behavior of different cooling solutions.

The experiments demonstrated in this work assume an active air-cooled heatsink. The value of the HTC of an air-cooled heatsink is determined by:

$$h_{eq} = \frac{h_{avg} \cdot A_t \cdot \left(1 - \frac{N \cdot A_f \cdot (1 - \eta_f)}{A_t}\right)}{LW} \quad (3)$$

where  $A_t$  is the total area of the heatsink,  $A_f$  is the fin area,  $N$  is the number of fins,  $\eta_f$  is the fin efficiency, and  $L$  and  $W$  are the length and width of the base plate. The average convective HTC ( $h_{avg}$ ) can be calculated using the Nusselt number [30]. We select values consistent with a basic copper heatsink with forced airflow provided by a typical commercial computer fan.

While an active air-cooled heatsink is assumed in this work, similar equations to Equation 3 for liquid cooling exist [30]. If the system designer chose to use liquid cooling for the simulation, a new HTC would be calculated and applied in place of the air cooling HTC described previously.

While the above method of abstracting a heatsink is effective for systems where heat is dissipated primarily through the external boundaries of the package (top of the lid, bottom of the substrate), a different modeling approach may be used for other cooling methods, such as inter-tier liquid cooling, where microchannels contact the chip directly [24, 29]. In such an approach, heat is dissipated directly from the chip without moving to a heat spreader like the lid. Hence, additional heat transfer coefficients or abstraction techniques may be needed to capture the cooling behavior.

### 4.3 FEM to Thermal RC models

This section describes the process of constructing a thermal RC model from the geometry of a given package. MFIT applies this technique to both 2.5D and 3D systems demonstrating the flexibility of the proposed methodology to different packaging technologies. However, this process can easily be applied to any package. Table 5 provides the notation of the equations used in this and the following subsection.

The package is first divided into horizontal layers, with the slicing process starting at the bottom substrate layer and ending at the top lid layer. Depending on the package design, each layer may be composed of a uniform material or various material blocks, resulting in either homogeneous or *non-homogeneous layers*. This flexibility enables the thermal RC model to simulate packages with heterogeneous designs where different chiplets are manufactured with various technologies, resulting in different material parameters in the same layer. Layers with uniform material properties are divided into a 2D grid of nodes, where the grid granularity can vary between layers. For non-homogeneous layers with different material blocks, each block can have a distinct grid granularity, resulting in a *non-uniform grid* that connects the entire package as a 3D network of thermal nodes, discretizing the chiplet geometry in space.

Since a layer or material blocks may have *anisotropic material*, where thermal conductivity differs along the x, y, and z axes (represented by  $k_x$ ,  $k_y$ , and  $k_z$ ), we calculate the thermal conductance ( $G_x$ ,  $G_y$ ,  $G_z$ ) for each node using the following equations:

$$G_x = \frac{k_x \cdot l_y \cdot l_z}{l_x}, G_y = \frac{k_y \cdot l_x \cdot l_z}{l_y}, G_z = \frac{k_z \cdot l_x \cdot l_y}{l_z} \quad (4)$$

where  $l_x$  and  $l_y$  are the node lengths in the x and y dimensions, respectively, and  $l_z$  represents the thickness of the layer. The thermal capacitance of each node is then calculated as  $C = \rho \cdot C_v \cdot l_x \cdot l_y \cdot l_z$ , where  $\rho$  is material density and  $C_v$  is the volumetric specific heat.

Heat is dissipated from the package primarily through a heatsink which is simulated using a convective heat transfer coefficient as detailed in Section 4.2.3. MFIT assumes forced convection is applied to the heatsink while passive convection occurs on the other external boundaries of the package. Consequently, convective conductance ( $G_{conv} = h_{eq} \cdot l_x \cdot l_y$ ) is incorporated into the nodes of the top and bottom layers.

The conductance between neighboring nodes  $i$  and  $j$  ( $G_{ij}$ ) of the same layers is determined by lateral conductance ( $G_x$  and  $G_y$ ). Since our thermal RC model allows non-uniform grid sizes for different layers and blocks, a node in one layer can be connected to multiple nodes from adjacent layers. Thus, vertical conductance between nodes of different layers is calculated from  $G_z$ , considering the overlap in the x-y plane. Once this RC network is

Table 5. Summary of the key parameters used in this work.

Notation	Definition
$k_x, k_y, k_z$	Thermal conductivity of a layer along the x, y, and z axes
$G_x, G_y, G_z$	Thermal conductance of a node along the x, y, and z axes
$\rho$	Material density
$C_v$	Volumetric specific heat of a layer
$G_{conv}$	Convection conductance of a boundary node
$h_{eq}$	Heat transfer coefficient of heatsink
$N$	Total number of nodes in the RC and DSS models
$T, \dot{T}$	$N \times 1$ temperature matrix and its derivative
$\dot{q}$	$N \times 1$ matrix of heat generation
$C, G$	$N \times N$ thermal capacitance and conductance matrices

established, we can formulate an ODE based on Kirchhoff's current law for a node  $i$  as:

$$C_i \frac{dT_i}{dt} = \sum_{j=1}^N (G_{ij})(T_j - T_i) + \dot{q}_i \quad (5)$$

where  $G_{ij} = 0$ , if  $i = j$  or  $j$  is not a neighbor node of  $i$ .

The heat generation ( $\dot{q}_i$ ) from node  $i$  is analogous to electric current, and temperature ( $T_i$ ) is analogous to voltage. Since only the chiplet layers consume power, heat generation for the nodes in other layers is zero. Solving the system of ODEs by forming a matrix is a well-studied approach. It can be represented by:

$$\mathbf{C} \times \dot{\mathbf{T}} = \mathbf{G} \times \mathbf{T} + \dot{\mathbf{q}} \quad (6)$$

where  $\mathbf{T}$ ,  $\dot{\mathbf{T}}$ , and  $\dot{\mathbf{q}}$  are  $N \times 1$  matrices representing node temperatures, temperature derivative, and generated heat.  $\mathbf{C}$  is a  $N \times N$  diagonal matrix, where each element corresponds to a node's thermal capacitance. The conductance matrix  $\mathbf{G}$  can be expressed as:

$$\mathbf{G} = \begin{bmatrix} -\sum_{j=1}^N G_{1j} & G_{12} & \cdots & G_{1N} \\ G_{21} & -\sum_{j=1}^N G_{2j} & \cdots & G_{2N} \\ \vdots & \vdots & \ddots & \vdots \\ G_{N1} & G_{N2} & \cdots & -\sum_{j=1}^N G_{Nj} \end{bmatrix} \quad (7)$$

where,  $G_{ij}$  represents conductance between the neighboring nodes  $i$  and  $j$ .

MFIT employs the backward Euler method to solve this system of ODEs, as its implicit formulation ensures stability when handling the stiff equations typical of thermal modeling. Given that the system's matrices are highly sparse (each node connects to only a few neighbors), MFIT leverages this sparsity by integrating SuperLU [33] as a sparse linear solver. Additionally, we incorporate the BLAS library [1] alongside SuperLU to further accelerate computations. To balance flexibility and performance, we implement the front-end in Python to define the geometry and ODE Equations, while the core computations rely on optimized C-based implementations of SuperLU.

**Capacitance Tuning:** While the thermal RC method provides very accurate steady-state temperature predictions, transient temperature calculations can exhibit relatively higher errors. This is a limitation of existing approaches as discussed in the experimental evaluations. To mitigate this issue, we fine-tune the capacitance values of each layer in the system using FEM results as a reference. Specifically, we introduce a scalar multiplier for each layer's capacitance and optimize these values using the nonlinear optimizer Nelder-Mead [7]. This tuning process is performed on a small-scale system and is based on the number of layers and their material properties rather than chiplet placement or geometry. Once optimized, the same capacitance parameters are applied to larger system sizes for more accurate thermal modeling without increasing grid complexity, as we demonstrate in Section 5.4. Since most advanced packaging technologies rely on similar materials, *re-tuning is rarely required*. Tuning is only necessary when the number of layers or material properties changes, in which case fine-tuning capacitance values on a small-scale system ensures accurate temperature calculation. In this work, we tune two representative small-scale systems, one for 2.5D systems and one for 3D system. The capacitance values of these representative systems are applied to the larger systems shown in the experimental results.

#### 4.4 Thermal RC to Discrete State Space models

The thermal RC model can be discretized in the time domain to further reduce the execution time of the model with no cost of accuracy. The discretization of a thermal RC model is completed by automated tools and takes only milliseconds to run. The DSS model can be used for dynamic thermal management applications where the

geometry is fixed, and faster thermal prediction is more important. However, a limitation of the DSS model is its dependence on an underlying continuous time model. It cannot be constructed directly without a thermal RC model as an intermediate step or system identification and measurement data. Additionally, a DSS model is specific to the geometry, materials, and sampling period used during the creation of the thermal RC model and the later discretization process. Therefore, the DSS model must be reconstructed if any design parameter changes. Only an existing RC model and a set time step are required to create a DSS model, with no direct information from the previous FEM model being needed.

Rearranging the Equation 6 into a state-space representation:

$$\dot{\mathbf{T}} = \mathbf{A}\mathbf{T} + \mathbf{B}\dot{\mathbf{q}}, \quad \text{where } \mathbf{A} = \mathbf{C}^{-1}\mathbf{G}, \quad \mathbf{B} = \mathbf{C}^{-1}. \quad (8)$$

The time evolution of this system over an interval  $t \in [kT_s, (k+1)T_s]$ , where  $T_s$  denotes the sampling period, is determined by solving the differential equation.

In the absence of power ( $\dot{\mathbf{q}} = 0$ ), the homogeneous solution is given as:

$$\mathbf{T}(t) = e^{\mathbf{A}(t-kT_s)}\mathbf{T}(kT_s) \quad (9)$$

Assuming  $\dot{\mathbf{q}}$  is present and remains constant over the interval under a zero-order hold (ZOH) approximation, the particular solution is given as:

$$\mathbf{T}(t) = \int_{kT_s}^t e^{\mathbf{A}(t-\tau)}\mathbf{B}\dot{\mathbf{q}}(\tau) d\tau \quad (10)$$

Combining Equations 9 and 10:

$$\mathbf{T}(t) = e^{\mathbf{A}(t-kT_s)}\mathbf{T}(kT_s) + \int_{kT_s}^t e^{\mathbf{A}(t-\tau)}\mathbf{B} d\tau \cdot \dot{\mathbf{q}}(kT_s) \quad (11)$$

Evaluating at  $t = (k+1)T_s$ , the system is discretized as:

$$\mathbf{T}((k+1)T_s) = e^{\mathbf{A}T_s}\mathbf{T}(kT_s) + \left( \int_0^{T_s} e^{\mathbf{A}\tau} d\tau \right) \mathbf{B}\dot{\mathbf{q}}(kT_s), \quad \text{where } \int_0^{T_s} e^{\mathbf{A}\tau} d\tau = \mathbf{A}^{-1}(e^{\mathbf{A}T_s} - \mathbf{I}) \quad (12)$$

Then, the discrete-time system matrices is defined as:

$$\mathbf{A}_d = e^{\mathbf{A}T_s}, \quad \mathbf{B}_d = \mathbf{A}^{-1}(\mathbf{A}_d - \mathbf{I})\mathbf{B} \quad (13)$$

the resulting discrete-time state-space equation is given by:

$$\mathbf{T}[k+1] = \mathbf{A}_d\mathbf{T}[k] + \mathbf{B}_d\dot{\mathbf{q}}[k] \quad (14)$$

Equation 14 represents the discrete-time equivalent of the continuous-time thermal RC model (shown in Equation 6). MFIT uses the zero-order hold (ZOH) method as given in Equation 10 for the discretization process. When power is provided as discrete inputs at each sampling period, ZOH provides an exact match to the continuous time model.  $T_s$  can be determined for discretization as a function of input power consumption and system dynamics.

*The DSS model consists only of multiply-accumulate operations, allowing for extremely fast operation, as shown in Section 5. The discretization process has only a one-time cost and is also nearly instantaneous, allowing for rapid DSS model creation when a thermal RC model is available.*

## 5 EXPERIMENTAL RESULTS

### 5.1 Experimental Setup

We evaluate the accuracy of the proposed MFIT methodology on three 2.5D systems and one 3D system representative of their respective classes. Three separate 2.5D systems are studied to demonstrate the flexibility of the proposed approach for systems with different numbers of chiplets. A 3D system is considered to demonstrate the capability of the approach to model systems beyond a single planar layer of chiplets. *Our thermal RC and DSS models are open-sourced to catalyze research in this domain.* The rest of this section describes the parameters and geometry of the 2.5D and 3D systems considered in this paper.

**5.1.1 Package Overview.** Both the 2.5D and 3D systems utilize a silicon interposer with chiplets placed upon it. The interposer is connected to the underlying substrate using C4 bumps. A copper lid covers the chiplets and acts as a heat spreader. The lid and substrate form the outer bounds of the package. Dimensions of the package for each system configuration are found in Table 6. Within the package, copper wires embedded in the interposer are used to connect neighboring chiplets. In both our 2.5D and 3D systems, each chiplet area is considered to be  $2.25\text{mm}^2$ , consistent with prior studies [27, 47, 48]. Each chiplet consists of multiple blocks. Each of these blocks corresponds to a component, such as a computational tile or a router used for inter-chiplet communication, as detailed in Figure 1a. Each of these blocks which make up the chiplet has an individual power profile. This means that different power profiles can be applied to every computational tile and router port in each chiplet. In our experimentation, different levels of detail are applied to the chiplets in the 2.5D and 3D systems as described in the following sections.

**2.5D System Specifics:** The target 2.5D system consists of a grid of chiplets integrated on an interposer, as illustrated in Figure 1a. Each chiplet is connected directly to the interposer via  $\mu$ -bumps surrounded by a capillary underfill material. The physical dimensions of the router ports are compatible with Universal Chiplet Interconnect Express (UCIe) specification [46]. The entire package is covered by a copper lid, which contacts each chiplet through a thermal interface material (TIM).

**3D System Specifics:** In the 3D system, three stacked chiplets are placed in a  $4 \times 4$  grid with equal spacing, consistent with [10]. Vertically stacked chiplets are connected to one another with  $\mu$ -bumps surrounded by a

Table 6. Specifications of simulated systems in this work

Parameter	16 2.5D	36 2.5D	64 2.5D	16x3 3D
<b>Package Geometry</b>				
Package Thickness (mm)	1.855	1.855	1.855	2.105
Package Length and Width (mm)	15.5	21.5	27.5	15.5
Package Top Area ( $\text{mm}^2$ )	240.25	462.25	756.25	240.25
Package Volume ( $\text{mm}^3$ )	445.66	857.47	1402.84	505.72
<b>Power (100% utilization)</b>				
Individual Chiplet Power (W)	3	3	3	1.2
Total System Power (W)	48	108	192	57.6
Total System Power per lid area ( $\text{W}/\text{mm}^2$ )	0.199	0.233	0.253	0.239
<b>Temperature</b>				
Maximum Chiplet Temperature ( $^{\circ}\text{C}$ )	118.25	129.75	164.03	142.01

capillary underfill material. The bottom chiplet of each stack is connected to the interposer with the same method. This integration is illustrated in Figure 1b. The lid contacts only the top chiplet layer through a thermal interface material.

## 5.2 Thermal RC Model Configuration

The number of nodes in the thermal RC network determines the model complexity, runtime, and granularity at which temperature can be observed in the model. A higher node density is used in chiplets to optimize this trade-off, while fewer nodes are used in non-chiplet components, such as the interposer, lid, substrate, and so on. Each chiplet is divided into four equal quadrants. One node is placed within each quadrant to allow for granular temperature monitoring across each chiplet. An alternate node density is used for non-chiplet layers in each model, as described below. This easily configurable non-uniform node density enables higher thermal resolution in critical parts such as chiplets while decreasing the runtime with lower resolution in less critical structures such as the substrate and lid. The DSS models in our experimentation are created by discretizing the thermal RC models with  $T_s = 0.01s$  sampling period. The sampling time can be chosen according to the application requirements.

**2.5D Thermal RC Model Specifics:** For the 2.5D systems, the choice of 4 nodes per chiplet leads to 64, 144, and 256 nodes in the chiplet layer of the 16, 36, and 64 chiplet systems, respectively. For all other layers, the number of nodes is equal to the total number of chiplets per layer. This allows the model to maintain higher thermal resolution in the critical chiplet layers while maintaining a fast execution time.

**3D Thermal RC Model Specifics:** The node densities in the 3D system are adjusted similarly to the 2.5D models. The layers that contain chiplets use an  $8 \times 8$  grid, implying 4 nodes per chiplet. All other layers have a  $4 \times 4$  grid, leading to a lower node density. The entire 3D system consists of 48 chiplets in total. There are a total of 192 nodes counting all nodes within chiplets.

**5.2.1 Input Workloads and Power Consumption.** Identical workloads are considered for the 2.5D and 3D systems, with differences in chiplet power density detailed in the following subsections. The target chiplet systems are analyzed under one synthetic (WL1) and five real AI/ML application workloads (WL2-WL6). The synthetic workload starts with a stress test that applies the maximum power to all chiplets to increase temperature beyond  $100^\circ\text{C}$ . Then, a pseudo-random bit sequence (PRBS) is applied to each chiplet to emulate a wide range of dynamic variations. Finally, all chiplets are turned off to let the temperature return to the ambient state, as depicted in Figure 9. Besides testing transient and steady-state behaviors, this power profile helps us to tune the thermal RC model.

The remaining scenarios consider processing-in-memory (PIM)-based chiplets for accelerating ML workloads. The computational platform is resistive random access memory (ReRAM) based chiplets commonly used in literature [44, 47, 51]. We select this configuration due to its ability to efficiently implement matrix-vector multiplication, which is the predominant operation in any CNN workload. Each workload consists of a series of deep neural networks (DNNs) which run in series on the system. The workloads are listed in Table 7. The neural networks (NN) in these workloads consist of several networks such as ResNets, DenseNets, and VGG networks. For example, WL1 contains 16 ResNet34's, followed by one VGG19, then 5 ResNet50's, and so on. Each workload contains from 20 to 40 individual networks. Workloads are mapped to the system as computing resources become available, meaning a new NN is mapped to chiplets when it completes the execution of a previous NN. Consequently, these workloads consist of NNs ranging from small NNs like ResNet18, which can be mapped to a single chiplet, to larger NNs such as DenseNet169, which are spread across multiple chiplets.

After mapping the group of NNs to the target chiplet-based systems, the chiplet power consumption is estimated in two parts, communication and computation. We estimate computation power through NeuroSim and



interconnection network power using BookSim [13, 25]. We use running average power throughout the workload execution (40-55 seconds), consistent with power measuring tools such as Intel RAPL [17] and pyNVML [2].

**Differences in 2.5D and 3D system chiplet power:** Different hardware parameters, such as voltage and frequency, are used for the 2.5D and 3D systems. This results in lower per-chiplet power consumption in the 3D system of 1.2W as compared to 3W for the 2.5D system, detailed under the *Power* section of Table 6. Using these parameters, the total system power per lid area of the 3D system is between that of the 36 and 64 chiplet 2.5D system. This level means that the temperature of individual chiplets should be roughly equivalent between these systems, which is confirmed in Figure 9.

*5.2.2 Configuration of other thermal simulators:* We compare our proposed thermal RC and DSS models against the state-of-the-art analytical thermal modeling tools HotSpot [49], 3D-ICE [21], and PACT [57] for all system sizes and workload configurations. Since HotSpot was originally designed for 2D chips, we utilize an extension that incorporates 3D modeling capabilities [38] to support both 2.5D and 3D integrated systems. Identical geometry and material parameters are set across all tools, aligning them with our reference FEM model. None of these tools support thermal conductivity variations along the x, y, and z directions. Consequently, for anisotropic material layers (e.g., the C4 bump layer) in the chiplet package, we use an averaged thermal conductivity to approximate this configuration. Additionally, HotSpot and PACT do not allow non-uniform grid sizes across different horizontal layers, so a uniform grid size matching our chiplet layer is used. We configure the non-uniform grid in 3D-ICE [21] to be consistent with our thermal RC model, ensuring the same number of thermal nodes for each system. Additionally, PACT provides flexibility in solver selection by supporting various SPICE solvers from Xyce [23]. For consistency, we use the TRAP solver, as given in [57]. PACT also enables parallel execution, which we leverage by running all simulations with eight cores on an Intel 10700k CPU.

### 5.3 Execution Time Evaluation

This section evaluates the execution time of the proposed multi-fidelity thermal model set. All simulations are run on a dual Intel Xeon Gold 6242R system with 40 processing cores. We use WL1 for our timing analysis since the execution time is comparable across all workloads.

Table 7. Descriptions of the workloads used in this work. (C) denotes the CIFAR100 dataset, and (I) denotes the ImageNet dataset.

Workload	Composition
WL1	Synthetic (see Figure 9)
WL2	16×ResNet34 (C), 1×VGG19 (C), 5×ResNet50 (C), 3×DenseNet40 (C), 1×ResNet152 (C), 1×VGG19 (I), 4×ResNet34 (I), 1×ResNet18 (I), 1×ResNet50 (I), 1×VGG16 (I)
WL3	16×ResNet34 (I), 1×VGG19 (I), 5×ResNet50 (I), 3×DenseNet169 (I), 1×ResNet110, 1×VGG19 (I), 4×ResNet101 (I), 1×ResNet152 (I), 1×ResNet18 (I), 1×ResNet50 (I), 1×Resnet152 (I)
WL4	16×ResNet34 (C), 2×VGG19 (I), 4×DenseNet169 (I), 3×DenseNet40 (C), 5×ResNet50 (C), 3×ResNet101, 7×ResNet150 (I), 2×VGG19 (I), 4×ResNet101, 1×VGG19 (C)
WL5	16×Resnet34 (I), 1×ResNet152 (I), 1×ResNet110 (I), 3×ResNet101 (I), 9×DenseNet169 (I), 4×ResNet34 (I), 12×ResNet18 (I), 5×ResNet50 (I), 1×ResNet152 (I)
WL6	3×DenseNet169 (I), 4×ResNet34 (I), 12×ResNet18 (I), 4×ResNet101 (I), 2×VGG19 (I), 4×ResNet101 (I), 1×VGG19 (C), 3×DenseNet40 (C)

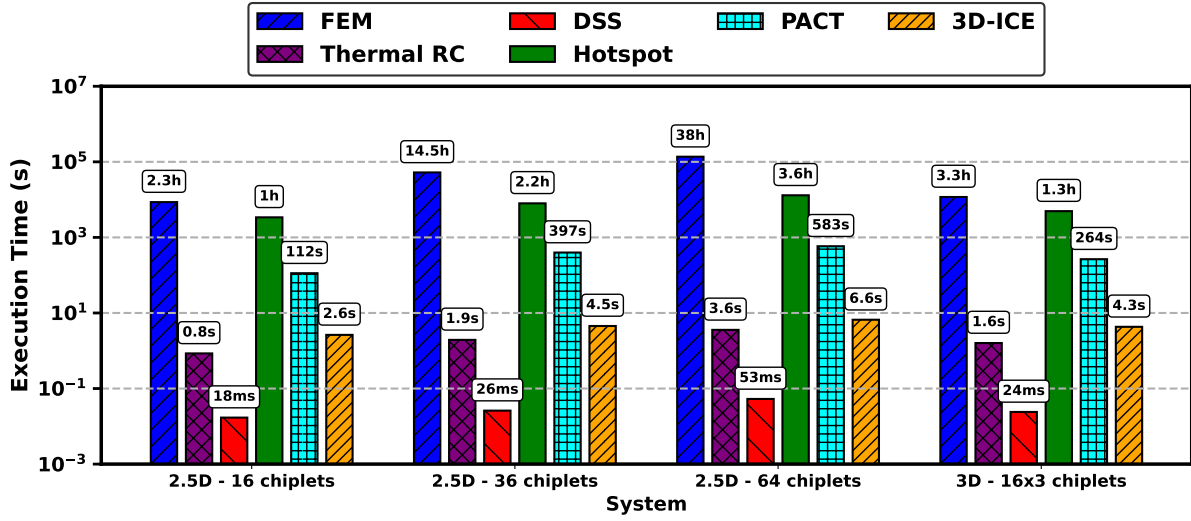


Fig. 8. Execution times (in log scale) of the proposed thermal models and HotSpot [49], PACT [57], and 3D-ICE [52] for 16, 36, 64 - 2.5D integrated and 16x3 - 3D integrated chiplet systems.

**2.5D Evaluation:** Abstracted FEM simulations take 2.4, 14.5, and 38.0 hours for 16, 36, and 64 chiplet systems, respectively. While providing an accurate reference, these long simulation times and significant development effort make FEM impractical for DSE. Our thermal RC models fill this gap with execution times ranging from 0.85 to 3.57 seconds for 16, 36, and 64 chiplets, as summarized in the first 3 systems in Figure 8. Coupled with the accuracy presented in the Section 5.4, the 10,000 to 40,000-fold speedup demonstrates their viability as a DSE tool.

Thermal RC models are derived directly from the underlying geometry and material parameters, meaning they can be reconfigured for different hardware and design configurations without re-calibration from FEM simulations. Relaxing this physical system to model connection, our DSS models reduce execution time to 18, 26, and 54 milliseconds for 16, 36, and 64 chiplets respectively. This speedup with respect to the RC model enables runtime temperature prediction, which can inform dynamic thermal power management (DTPM) decisions to increase system performance and reliability [11]. While maintaining the accuracy for a given configuration, DSS can be regenerated from the RC model in a few milliseconds if the sampling period or hardware configuration changes.

**3D Evaluation:** The execution time results of the 3D system are summarized in the 3D - 16x3 chiplet system of Figure 8. FEM simulations take approximately 3.3 hours for the single 3D system. The thermal RC model significantly reduces the runtime to 1.6 seconds. Similar to the 2.5D system, the 3D DSS model further reduces runtime to just 24 milliseconds. This substantial speedup is due to the DSS model relying solely on matrix multiplication operations, which are highly optimized on modern hardware through SIMD instructions and other acceleration techniques, such as efficient memory access.

**Execution time comparison to existing tools:** The commonly used thermal modeling tools, HotSpot [50], 3D-ICE [21], and PACT [57] belong to the same class of model as our thermal RC models. As shown in Figure 8, our proposed thermal RC and DSS methods achieve significantly faster execution times compared to these tools.

HotSpot and PACT, both of which lack support for non-uniform grids, leading to more complex ODE formulations and increased computational overhead. Additionally, HotSpot relies on the computationally expensive

RK4 solver, while PACT, designed for transistor-level simulations, introduces further overhead due to its reliance on the Xyce solver. As a result, our thermal RC model achieves a  $4235\times$  speedup for 16 chiplets,  $4082\times$  for 36 chiplets,  $3630\times$  for 64 chiplets, and  $4050\times$  for the  $16\times 3$  3D chiplet system compared to HotSpot. Against PACT, our thermal RC model is  $132\times$  faster for 16 chiplets,  $205\times$  for 36 chiplets,  $164\times$  for 64 chiplets, and  $167\times$  for the  $16\times 3$  3D chiplet system.

While 3D-ICE supports non-uniform grids, our thermal RC model still outperforms it by leveraging the Backward Euler method with SuperLU and BLAS libraries for an efficient ODE solver. Consequently, our approach achieves a  $3\times$  speedup for 16 chiplets,  $2.3\times$  for 36 chiplets,  $1.9\times$  for 64 chiplets, and  $2.7\times$  for the  $16\times 3$  3D chiplet system over 3D-ICE. Moreover, our DSS method surpasses all RC-based models in execution efficiency, demonstrating the best performance among all evaluated tools. Finally, we emphasize that MFIT, our multi-fidelity thermal model set, covers a *much wider range of accuracy and execution time trade-offs* than a specific point solution, providing greater flexibility for different modeling needs.

#### 5.4 Validation of Thermal RC and DSS model

We validate the accuracy of our thermal RC and DSS models by comparing their temperature estimates to full-system FEM simulation results for the same workload and system configurations. This comparison is completed for each of the three 2.5D system sizes and the single 3D system. In addition to the visualization of the temperature estimate over time, shown in Figure 9, two metrics are used to quantify the accuracy of our thermal RC and

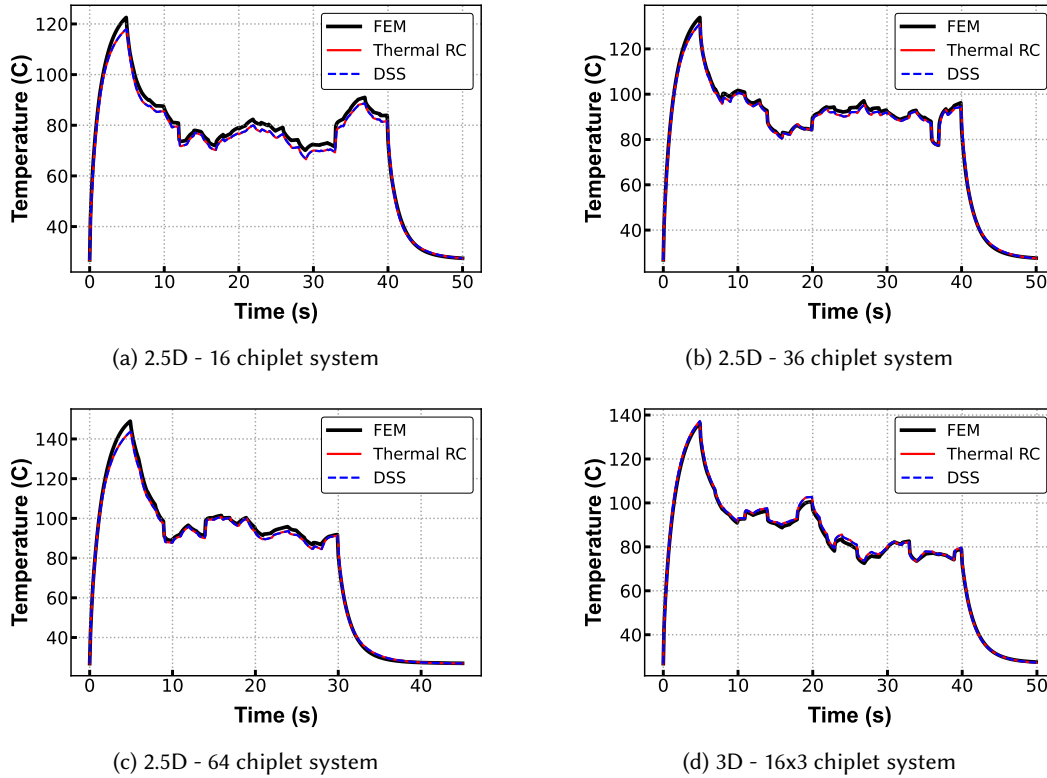


Fig. 9. Temperature vs. Time of representative chiplets from 2.5D and 3D systems. WL1 is shown for all systems.

DSS models against the FEM results. The MAE metric measures the mean absolute error in temperature across the entire simulation duration. The second metric, Temperature Violation Prediction accuracy, measures the accuracy of our models in predicting temperature violations. Predicting temperature violations (e.g., tracking the time steps when the temperature exceeds the allowed threshold) is often used by DTPM algorithms. We set 85°C as the maximum allowable temperature threshold for each system without loss of generality [62]. This metric first identifies the time steps in FEM simulations where temperature violations occur (temperature exceeds 85°C). Then, it computes the percentage of these violations captured by the thermal RC and DSS models (e.g., 100% means all violations are detected with perfect accuracy). The proposed models conservatively flag violations within one degree of the above-mentioned threshold temperature.

To assist users in visualizing the thermal behavior of the system under test, the RC model also creates a heat map of each layer in the system. As an example, the heat map of the interposer layer of a 2.5D 64 chiplet system is shown in Figure 10. This figure shows the temperature gradient that occurs between the center of the interposer, where the heat-producing chiplets are located, and the edges of the system, where there are no chiplets. These maps allow for quick visual verification of the system behavior instead of relying purely on numerical results.

**2.5D Validation Results:** Figures 9a, 9b, and 9c plot the temperature as a function of time for each 2.5D system size of a representative chiplet while running workload WL1. All three plots of 2.5D systems clearly show that the systematically constructed thermal RC and DSS models produce near-identical results to the FEM baseline. They closely follow the FEM results during the stress test (temperature increases until reaching the maximum point), randomly changing chiplet power consumption (middle portion), and cool-down periods.

The first 3 columns of Table 8 summarize the accuracy results for all 2.5D systems and workloads. The worst-case mean absolute error of our models are only 1.46, 1.64, and 1.35 degrees for 16, 36, and 64 chiplet systems,

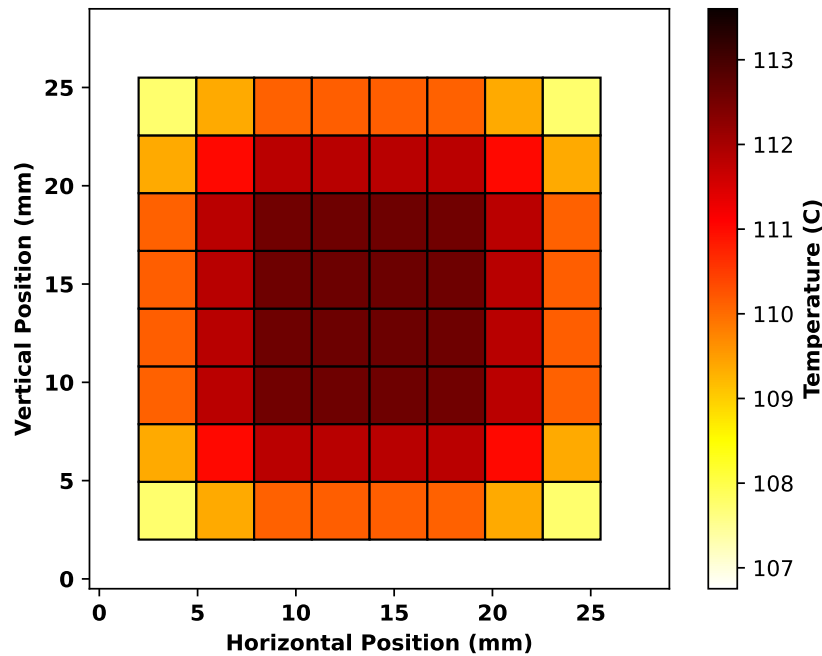


Fig. 10. A heat map of the interposer layer generated by thermal RC model.

Table 8. Mean Absolute Error and accuracy in predicting temperature violations are shown as compared to reference FEM results. The thermal RC, DSS, HotSpot [49], 3D-ICE[52], and PACT [57] models are shown. Best MAE for each system-workload combination are highlighted in red. **Average operating temperatures are in the range of 60-80 (°C).**

Workload	Model	2.5D - 16 Chiplets		2.5D - 36 Chiplets		2.5D - 64 Chiplets		3D - 16x3 Chiplets	
		MAE (°C)	Temp. Violation Accuracy (%)	MAE (°C)	Temp. Violation Accuracy (%)	MAE (°C)	Temp. Violation Accuracy (%)	MAE (°C)	Temp. Violation Accuracy (%)
WL1	Thermal RC	<b>1.23</b>	93.5	<b>1.42</b>	96.9	<b>0.99</b>	100.0	<b>0.94</b>	98.1
	DSS	<b>1.23</b>	93.5	<b>1.42</b>	96.9	<b>0.99</b>	100.0	<b>0.94</b>	98.1
	HotSpot	2.74	67.8	1.64	97.0	2.16	96.9	2.37	87.6
	3D-ICE	1.65	89.5	2.07	98.0	1.65	99.6	1.73	97.7
	PACT	1.99	91.7	1.61	99.2	1.70	99.4	2.09	99.0
WL2	Thermal RC	<b>0.86</b>	96.0	1.16	78.48	<b>0.95</b>	95.83	<b>0.98</b>	100.0
	DSS	<b>0.86</b>	96.0	1.16	78.48	<b>0.95</b>	95.83	<b>0.98</b>	100.0
	HotSpot	1.58	75.0	1.24	29.74	1.01	67.36	1.74	100.0
	3D-ICE	1.36	85.1	1.35	3.79	1.82	76.38	1.39	100.0
	PACT	1.58	75.9	<b>0.91</b>	23.41	1.55	66.66	2.10	100.0
WL3	Thermal RC	<b>1.02</b>	100.0	1.28	77.3	<b>1.03</b>	97.0	<b>0.80</b>	100.0
	DSS	<b>1.02</b>	100.0	1.28	77.3	<b>1.03</b>	97.0	<b>0.80</b>	100.0
	HotSpot	1.97	100.0	1.18	42.4	1.12	72.3	1.79	100.0
	3D-ICE	1.15	100.0	1.53	14.9	1.82	80.7	1.12	100.0
	PACT	2.03	100.0	<b>1.09</b>	42.4	1.75	72.3	1.80	100.0
WL4	Thermal RC	<b>1.46</b>	96.6	<b>1.64</b>	95.6	<b>1.35</b>	96.8	<b>1.48</b>	98.5
	DSS	<b>1.46</b>	96.6	<b>1.64</b>	95.6	<b>1.35</b>	96.8	<b>1.48</b>	98.5
	HotSpot	2.29	95.6	7.39	92.0	2.10	96.5	2.71	96.7
	3D-ICE	3.72	91.3	2.33	97.0	2.68	97.4	2.46	96.8
	PACT	3.56	93.8	1.94	97.7	2.39	97.4	2.97	96.6
WL5	Thermal RC	<b>1.01</b>	100.0	1.25	87.9	<b>0.96</b>	82.9	<b>0.87</b>	100.0
	DSS	<b>1.01</b>	100.0	1.25	87.9	<b>0.96</b>	82.9	<b>0.87</b>	100.0
	HotSpot	1.95	100.0	1.16	60.7	1.30	2.9	1.86	100.0
	3D-ICE	1.16	100.0	1.53	20.0	1.79	48.6	<b>0.87</b>	100.0
	PACT	1.99	100.0	<b>1.13</b>	53.2	1.87	17.1	1.64	100.0
WL6	Thermal RC	<b>0.89</b>	98.1	1.30	84.8	<b>1.21</b>	92.8	<b>1.52</b>	94.0
	DSS	<b>0.89</b>	98.1	1.30	84.8	<b>1.21</b>	92.8	<b>1.52</b>	94.0
	HotSpot	1.62	85.9	<b>1.28</b>	89.8	1.48	77.2	2.22	81.4
	3D-ICE	1.34	91.8	1.69	78.5	2.38	76.2	1.61	74.9
	PACT	1.67	89.3	1.28	91.7	1.85	92.8	2.43	69.8

respectively. These results indicate that the proposed models achieve excellent accuracy across different hardware configurations and workloads. Our models also achieve FEM-level high accuracy in predicting temperature violations as described earlier in Section 5.4. For example, the worst-case accuracy for the 16-chiplet system is 93.5% (i.e., only 6.5% of the time steps where violations are missed). With the exception of WL2 and 3, prediction accuracy exceeds 82% for all other workloads run on the 36 chiplet system. The same trend is seen with the 64 chiplet system.

For some specific workload-system combinations, such as WL2 and 3 run on the 36 chiplet system, prediction accuracy falls below the 80% mark for our models. These relatively lower accuracy values stem from sudden temperature spikes that lead to short-term temperature violations in these workload-system combinations. Temperature spikes in specific chiplets occur when several grouped chiplets experience a transient power spike simultaneously. This increases the temperature of the more central chiplets in the group. In these cases, the peak temperatures are mostly at or below 85 degrees with infrequent short-term violations, which can be tolerated. For example, FEM simulations indicate only 255 temperature violations across all chiplets in WL3 compared to 11 thousand violations in WL1. Hence, missing even a few violations impacts the accuracy heavily when the RC and DSS models do not capture these spikes. In contrast, our thermal RC and DSS models effectively detect more prolonged violations, as evidenced by WL1, WL3, WL4, WL5, and WL6.

**3D Validation Results:** Figure 9d plots the temperature as a function of time for the single 3D system of a representative chiplet running WL1. The plot shows similar behavior to the 2.5D comparison, where the RC and DSS match each other exactly and match the reference FEM results extremely closely during the stress test, random, and cool-down portions of the workload.

The far right column of Table 8 summarizes the accuracy results for the single 3D system for each workload. The worst-case MAE is only 1.52 degrees. This result shows that the proposed models maintain high levels of accuracy even when applied to a stacked die package. This high degree of accuracy is repeated when predicting temperature violations. The worst case temperature violation prediction accuracy is only 94.0%, occurring for workload 6.

**Accuracy comparison to existing tools:** Table 8 also lists the MAE of HotSpot, 3D-ICE, and PACT simulations compared to FEM simulations for the 2.5D and 3D systems. For the 2.5D system results, the average error of Hotspot, 3D-ICE, and PACT across all workloads are 0.7, 0.66, and 0.59 degrees greater than our thermal RC and DSS models. For the 3D system results, the average error of Hotspot, 3D-ICE, and PACT across all workloads are 1.02, 0.43, and 1.07 degrees greater than our thermal RC and DSS models.

There are several reasons for the improved accuracy of our models as compared to existing thermal modeling tools. First, PACT and 3D-ICE are not able to model convective heat transfer from more than one boundary of the package. In the case of 3D-ICE, this configuration would require a uniform grid node distribution, which would negatively impact execution time. Second, none of these existing simulators support the ability to provide different thermal conductivities along the x, y, and z-axis, further decreasing accuracy. Third, our models have their node capacitance values tuned, improving their transient thermal simulation accuracy. Lastly, the strength of the PACT simulator is circuit-level thermal simulations. It assumes that the grid granularity would be much higher than the block granularity (i.e., there are many nodes per block). In architectural-level thermal simulations, which is the focus of this work, there are many fewer nodes per block. In the PACT simulator, this can result in uneven node distribution, leading to decreased accuracy.

## 6 CONCLUSION

Due to increasing manufacturing costs, conventional monolithic 2D chips cannot sustain the increasing performance and compute capacity demands. 2.5D and 3D chiplet systems have emerged as cost-effective solutions to continue the required scaling. However, substantial compute power in a small volume intensifies the power density, leading to severe heat dissipation and thermal challenges. There is a strong need for open-source thermal modeling tools that enable researchers to analyze thermal behavior and perform thermally aware optimizations. Re-purposing existing approaches developed for monolithic chips incurs accuracy and execution time penalties, while custom-designed singular solutions have limited scope. To fill this gap, this paper proposed MFIT, a set of multi-fidelity thermal models that span a wide range of accuracy and execution time trade-offs. Since the proposed models are consistent by construction, designers can use them throughout the design cycle, from system specification to design space exploration and runtime resource management.

## REFERENCES

- [1] [n. d.]. BLAS (Basic Linear Algebra Subprograms). <https://www.netlib.org/blas/>
- [2] [n. d.]. pyNVML. <https://github.com/gpuopenanalytics/pynvml>.
- [3] 2021. Semiconductor Research Corporation, "Decadal Plan for Semiconductors". <https://www.src.org/about/decadal-plan/decadal-plan-full-report.pdf>, Accessed on March 31, 2024.
- [4] Rahul Agarwal, Patrick Cheng, Priyal Shah, Brett Wilkerson, Raja Swaminathan, John Wu, and Chandrasekhar Mandalapu. 2022. 3D packaging for heterogeneous integration. In *2022 IEEE 72nd Electronic Components and Technology Conference (ECTC)*. IEEE, 1103–1107.
- [5] Hussam Amrouch and Jörg Henkel. 2015. Lucid infrared thermography of thermally-constrained processors. In *Proc. of IEEE/ACM ISLPED*. 347–352.

- [6] Semiconductor Industry Association. [n. d.]. Intl. Technology Roadmap for Semiconductors 2015 Edition. <https://www.semiconductors.org/resources/2015-Intl.-technology-roadmap-for-semiconductors-its/>.
- [7] Russell R Barton and John S Ivey Jr. 1996. Nelder-Mead simplex modifications for simulation optimization. *Management Science* 42, 7 (1996), 954–973.
- [8] Srikant Bharadwaj, Jieming Yin, Bradford Beckmann, and Tushar Krishna. 2020. Kite: A Family of Heterogeneous Interposer Topologies Enabled via Accurate Interconnect Modeling. In *Proc. of ACM/IEEE DAC*.
- [9] Ganapati Bhat, Gaurav Singla, Ali K. Unver, and Umit Y. Ogras. 2018. Algorithmic Optimization of Thermal and Power Management for Heterogeneous Mobile Platforms. *IEEE Trans. VLSI Syst.* 26, 3 (2018), 544–557.
- [10] Bryan Black, Murali Annavaram, Ned Brekelbaum, John DeVale, Lei Jiang, Gabriel H. Loh, Don McCaule, Pat Morrow, Donald W. Nelson, Daniel Pantuso, Paul Reed, Jeff Rupley, Sadasivan Shankar, John Shen, and Clair Webb. 2006. Die Stacking (3D) Microarchitecture. In *2006 39th Annual IEEE/ACM International Symposium on Microarchitecture (MICRO'06)*, 469–479. <https://doi.org/10.1109/MICRO.2006.18>
- [11] David Brooks, Robert P. Dick, Russ Joseph, and Li Shang. 2007. Power, Thermal, and Reliability Modeling in Nanometer-Scale Microprocessors. *IEEE Micro* 27, 3 (2007), 49–62.
- [12] Shengze Cai, Zhicheng Wang, Sifan Wang, Paris Perdikaris, and George Em Karniadakis. 2021. Physics-informed neural networks for heat transfer problems. *Journal of Heat Transfer* 143, 6 (2021), 060801.
- [13] Pai-Yu Chen, Xiaochen Peng, and Shimeng Yu. 2018. NeuroSim: A Circuit-Level Macro Model for Benchmarking Neuro-Inspired Architectures in Online Learning. *IEEE TCAD-IC* 37, 12 (2018), 3067–3080.
- [14] Y.-K. Cheng et al. 2020. Next-Generation Design and Technology Co-optimization (DTCO) of System on Integrated Chip (SoIC) for Mobile and HPC Applications. In *Proc. of IEEE IEDM*. 41.3.1–41.3.4.
- [15] Pavan Kumar Chundi et al. 2017. Hotspot monitoring and Temperature Estimation with miniature on-chip temperature sensors. In *Proc. of IEEE/ACM ISLPED*. 1–6.
- [16] COMSOL. [n. d.]. COMSOL Multiphysics Reference Manual. <https://comsol.com>. <https://www.comsol.com/>
- [17] Howard David et al. 2010. RAPL: Memory power estimation and capping. In *Proc. of the ACM/IEEE ISLPED*. 189–194.
- [18] Yasuko Eckert, Nuwan Jayasena, and Gabriel H Loh. 2014. Thermal feasibility of die-stacked processing in memory. In *Proc. of WoNDP*.
- [19] Furkan Eris, Ajay Joshi, Andrew B. Kahng, Yenai Ma, Saiful Mojumder, and Tiansheng Zhang. 2018. Leveraging thermally-aware chiplet organization in 2.5D systems to reclaim dark silicon. In *2018 Design, Automation & Test in Europe Conference & Exhibition (DATE)*. 1441–1446. <https://doi.org/10.23919/DATE.2018.8342238>
- [20] Yongkui Han, Israel Koren, and C Mani Krishna. 2007. TILTS: A fast architectural-level transient thermal simulation method. *Journal of Low Power Electronics* 3, 1 (2007), 13–21.
- [21] Darong Huang, Luis Costero, and David Atienza. 2024. An Evaluation Framework for Dynamic Thermal Management Strategies in 3D MultiProcessor System-on-Chip Co-Design. *IEEE Transactions on Parallel and Distributed Systems* (2024).
- [22] Shih-Chang Huang, Hong-Ping Cheng, Chun-Kai Lo, Yung-Chuan Tseng, and Chin-Chi Cheng. 2023. Experimental study of a two-phase immersion cooling system for the CPU in a PC and a 2U server operated at the overclocking frequency. *IEEE Transactions on Components, Packaging and Manufacturing Technology* 13, 6 (2023), 859–864.
- [23] S Hutchinson, E Keiter, R Hoekstra, H Watts, A Waters, T Russo, R Schells, S Wix, and C Bogdan. 2002. The Xyce™ parallel electronic simulator—an overview. *Parallel Computing: Advances and Current Issues* (2002), 165–172.
- [24] Leslie Hwang, Beomjin Kwon, and Martin Wong. 2018. Accurate models for optimizing tapered microchannel heat sinks in 3D ICs. In *Proc. of IEEE Computer Society Annual Symposium on VLSI (ISVLSI)*. 58–63.
- [25] Nan Jiang et al. 2013. A detailed and flexible cycle-accurate network-on-chip simulator. In *Proc. of ISPASS*. IEEE, 86–96.
- [26] Waqar Ahmed Khan, J. Richard Culham, and M. Michael Yovanovich. 2008. Modeling of Cylindrical Pin-Fin Heat Sinks for Electronic Packaging. *IEEE Transactions on Components and Packaging Technologies* 31, 3 (2008), 536–545.
- [27] Gokul Krishnan et al. 2021. SIAM: Chiplet-based scalable in-memory acceleration with mesh for deep neural networks. *ACM Transactions on Embedded Computing Systems (TECS)* 20, 5s (2021), 1–24.
- [28] Gokul Krishnan et al. 2022. Big-Little Chiplets for In-Memory Acceleration of DNNs: A Scalable Heterogeneous Architecture. In *2022 IEEE/ACM ICCAD*. 1–9.
- [29] Beomjin Kwon, Faizan Ejaz, and Leslie K Hwang. 2020. Machine learning for heat transfer correlations. *International Communications in Heat and Mass Transfer* 116 (2020), 104694.
- [30] Theodore L. Bergman, Adrienne S. Lavine, Frank P. Incropera, and David P. DeWitt. 2011. *Fundamentals of Heat and Mass Transfer*. John Wiley & Sons.
- [31] John H Lau. 2023. *Chiplet design and heterogeneous integration packaging*. Springer.
- [32] Fuping Li, Ying Wang, Yuanqing Cheng, Yujie Wang, Yinhe Han, Huawei Li, and Xiaowei Li. 2022. GIA: A Reusable General Interposer Architecture for Agile Chiplet Integration. In *Proceedings of the 41st IEEE/ACM International Conference on Computer-Aided Design (San Diego, California) (ICCAD '22)*. Association for Computing Machinery, New York, NY, USA, Article 42, 9 pages. <https://doi.org/10.1145/3508352.3549464>



- [33] Xiaoye S Li. 2005. An overview of SuperLU: Algorithms, implementation, and user interface. *ACM Transactions on Mathematical Software (TOMS)* 31, 3 (2005), 302–325.
- [34] Yuquan Li, R Wayne Johnson, Rui Zhang, Phillip Henson, Patrick Thompson, Tejpal Hooghan, and Jeremias Libres. 2010. Ti/au die backside metallization for flip chip heat spreader attachment. *IEEE transactions on electronics packaging manufacturing* 33, 1 (2010), 44–54.
- [35] Gian Luca Loi et al. 2006. A thermally-aware performance analysis of vertically integrated (3-D) processor-memory hierarchy. In *Proc. of DAC*. 991–996.
- [36] Yenai Ma, Leila Delshadtehrani, Cansu Demirkiran, José L Abellan, and Aiav Joshi. 2021. TAP-2.5 D: A thermally-aware chiplet placement methodology for 2.5 D systems. In *Proc. of DATE*. IEEE, 1246–1251.
- [37] John E Matsson. 2023. *An Introduction to Ansys Fluent 2023*. Sdc Publications.
- [38] Jie Meng, Katsutoshi Kawakami, and Ayse K Coskun. 2012. Optimizing energy efficiency of 3-D multicore systems with stacked DRAM under power and thermal constraints. In *Proc. of DAC*. 648–655.
- [39] Samuel Naffziger et al. 2021. Pioneering Chiplet Technology and Design for the AMD EPYC™ and Ryzen™ Processor Families : Industrial Product. In *Proc. of ACM/IEEE ISCA*. 57–70.
- [40] S. Narasimhan and J. Majdalani. 2002. Characterization of compact heat sink models in natural convection. *IEEE Transactions on Components and Packaging Technologies* 25, 1 (2002), 78–86.
- [41] Gregory Nellis and Sanford Klein. 2008. *Heat transfer*. Cambridge university press.
- [42] Jaehyun Park, Alish Kanani, Lukas Pfromm, Harsh Sharma, Parth Solanki, Eric Tervo, Janardhan Rao Doppa, Partha Pratim Pande, and Umit Y Ogras. 2024. Thermal Modeling and Management Challenges in Heterogenous Integration: 2.5 D Chiplet Platforms and Beyond. In *2024 IEEE 42nd VLSI Test Symposium (VTS)*. 1–4.
- [43] Sherif Sadiqbatcha et al. 2019. Hot spot identification and system parameterized thermal modeling for multi-core processors through infrared thermal imaging. In *Proc. of DATE*. 48–53.
- [44] Yakun Sophia Shao et al. 2021. Simba: Scaling Deep-Learning Inference with Multi-Chip-Module-Based Architecture, In *Proc. of IEEE/ACM MICRO*. *Commun. ACM* 64, 6, 107–116.
- [45] Shervin Sharifi and Tajana Šimunić Rosing. 2010. Accurate direct and indirect on-chip temperature sensing for efficient dynamic thermal management. *IEEE TCAD-IC* 29, 10 (2010), 1586–1599.
- [46] Debendra Das Sharma, Gerald Pasdast, Zhiguo Qian, and Kemal Aygun. 2022. Universal chiplet interconnect express (UCIe): An open industry standard for innovations with chiplets at package level. *IEEE Transactions on Components, Packaging and Manufacturing Technology* 12, 9 (2022), 1423–1431.
- [47] Harsh Sharma et al. 2022. SWAP: A Server-Scale Communication-Aware Chiplet-Based Manycore PIM Accelerator. *IEEE TCAD-IC* 41, 11 (2022), 4145–4156.
- [48] Harsh Sharma et al. 2023. Florets for Chiplets: Data Flow-aware High-Performance and Energy-efficient Network-on-Interposer for CNN Inference Tasks. *ACM Transactions on Embedded Computing Systems* 22, 5s (2023), 1–21.
- [49] Kevin Skadron and otheers. 2004. Temperature-Aware Microarchitecture: Modeling and Implementation. *ACM Trans. Archit. Code Optim.* 1, 1 (mar 2004), 94–125.
- [50] Kevin Skadron, Mircea R. Stan, Karthik Sankaranarayanan, Wei Huang, Sivakumar Velusamy, and David Tarjan. 2004. Temperature-Aware Microarchitecture: Modeling and Implementation. *ACM Trans. Archit. Code Optim.* 1, 1 (mar 2004), 94–125. <https://doi.org/10.1145/980152.980157>
- [51] Linghao Song, Xuehai Qian, Hai Li, and Yiran Chen. 2017. Pipelayer: A pipelined reram-based accelerator for deep learning. In *Proc. of HPCA*. IEEE, 541–552.
- [52] Arvind Sridhar, Alessandro Vincenzi, David Atienza, and Thomas Brunschweiler. 2013. 3D-ICE: A compact thermal model for early-stage design of liquid-cooled ICs. *IEEE Trans. Comput.* 63, 10 (2013), 2576–2589.
- [53] Dylan Stow, Itir Akgun, Russell Barnes, Peng Gu, and Yuan Xie. 2016. Cost analysis and cost-driven IP reuse methodology for SoC design based on 2.5D/3D integration. In *Proc. of IEEE/ACM ICCAD*. 1–6.
- [54] Hameedah Sultan, Anjali Chauhan, and Smruti R. Sarangi. 2019. A Survey of Chip-level Thermal Simulators. *ACM Comput. Surv.* 52, 2, Article 42 (apr 2019), 35 pages.
- [55] Pruek Vanna-Iampikul, Lingjun Zhu, Serhat Erdogan, Mohanalingam Kathaperumal, Ravi Agarwal, Ram Gupta, Kevin Rinebold, and Sung Kyu Lim. 2023. Glass Interposer Integration of Logic and Memory Chiplets: PPA and Power/Signal Integrity Benefits. In *2023 60th ACM/IEEE Design Automation Conference (DAC)*. IEEE, 1–6.
- [56] Martin Won. 2023. *Agilex FPGAs Deliver a Game-Changing Combination of Flexibility and Agility for the Data-Centric World*. Technical Report. Intel.
- [57] Zihao Yuan et al. 2021. PACT: An extensible parallel thermal simulator for emerging integration and cooling technologies. *IEEE TCAD-IC* 41, 4 (2021), 1048–1061.
- [58] Francesco Zanini, David Atienza, Colin N. Jones, and Giovanni De Micheli. 2010. Temperature sensor placement in thermal management systems for MPSoCs. In *Proc. of ISCAS*. 1065–1068.

- [59] Florian Zaruba, Fabian Schuiki, and Luca Benini. 2020. A 4096-core RISC-V chiplet architecture for ultra-efficient floating-point computing. In *Proc. of IEEE Hot Chips 32 Symposium*. IEEE Computer Society, 1–24.
- [60] Jinwei Zhang et al. 2021. Full-chip power density and thermal map characterization for commercial microprocessors under heat sink cooling. *IEEE TCAD-IC*. 41, 5 (2021), 1453–1466.
- [61] Yufu Zhang, Ankur Srivastava, and Mohamed Zahran. 2008. Chip level thermal profile estimation using on-chip temperature sensors. In *IEEE Intl. Conf. on Computer Design*. 432–437.
- [62] Minxuan Zhou et al. 2020. Temperature-Aware DRAM Cache Management—Relaxing Thermal Constraints in 3-D Systems. *IEEE TCAD-IC* 39, 10 (2020), 1973–1986.
- [63] Minghao Zhou, Li Li, Fengze Hou, Guoqiang He, and Jiaqi Fan. 2022. Thermal Modeling of a Chiplet-Based Packaging With a 2.5-D Through-Silicon Via Interposer. *IEEE Transactions on Components, Packaging and Manufacturing Technology* 12, 6 (2022), 956–963.